Journal of Building Engineering 44 (2021) 103176

Contents lists available at ScienceDirect

Journal of Building Engineering

journal homepage: www.elsevier.com/locate/jobe

A design oriented fibre-based model for simulating the long-term behaviour of RC beams: Application to beams cast in different stages

Claudio Mazzotti, Nicola Buratti *

Department of Civil, Chemical, Environmental and Materials Engineering (DICAM), Alma Mater Studiorum - University of Bologna, Viale del Risorgimento 2, 40136, Bologna, Italy

ARTICLE INFO

Keywords:
Numerical model
Creep
Concrete
Precast-concrete
Experimental test
Shrinkage

ABSTRACT

The present paper describes a numerical model that has been developed in order to analyse the long-term behaviour of beams built in different stages under serviceability loads, considering the effect of delayed deformations due to creep and shrinkage. The rheological model for concrete creep is based on a modified version of the solidification theory while the cross section behaviour is described by means of a fibre model. The paper discusses the performances of the model in simulating the behaviour of two fullscale beams tested by the authors.

1. Introduction

Long term deformations may be extremely significant for reinforced concrete structures, in particular under serviceability conditions and for some particular classes of structures, e.g. very long span bridges, may even lead to structural collapse [1,2].

Many simple models are available for the analysis of creep and shrinkage deformations of reinforced concrete beams and frames with normal-length spans [3–7] but these models are not suitable for analyzing beams built in different stages in which there are concretes cast at different times which exhibit different delayed deformations. The analysis of the structural behaviour of such systems requires specific analytical models, which must be able to take different construction stages into account. In fact, due to the different ageing of the materials involved, the long-term behaviour of such structural elements can significantly differ from the predictions provided by conventional analytical methods such as AAEM, EM, etc. [5,7]. The study of the stress and deformation states of the beams may be complex, especially as far as serviceability limit states are concerned. In fact, the superposition principle cannot be used [8], neither to estimate the behaviour under service loadings nor to evaluate the ultimate bearing capacity, therefore time incremental formulations are required in order to obtain reliable results.

The present paper describes a numerical model that has been developed by the authors in order to analyse the long-term behaviour of beams built in different stages under serviceability loads, considering the effect of delayed deformations due to creep and shrinkage. The model is an extension of the nonlinear creep damage model, based on a modified version of the solidification theory [9], proposed by Mazzotti and Savoia [10], for concrete under uniaxial compression. The main improvements are: (*i*) the definition of a fibre based model for the analysis of cross sections; (*ii*) the inclusion of shrinkage effects at the cross section level; (*iii*) the ability to simulate the global behaviour of beams; and (*iv*) tension stiffening effects. An earlier version of the present model, which included the fibre-based cross section model only (*i*), was described in Refs. [11,12]. These former versions of the model were never validated against experimental data on the behaviour of structural elements.

In the model proposed part of the fibres are considered active only after a given time interval, in order to reproduce the different construction phases of the beams. Numerical simulations are carried out by calculating the curvature at the sectional level first and then evaluating the overall behaviour of the structural elements taking into account also tension stiffening. An incremental algorithm is formulated in order to describe the stress redistribution occurring when the portion of the concrete section cast in a subsequent step becomes effective. More complex structures such as very long span bridges are behind the scope of the present model and would require more complex approaches [1,2,13–16].

In particular, the model was used in order to simulate the results of an experimental campaign on the flexural behaviour of two beams built in two different stages. These beams are part of a construction system in

* Corresponding author.
E-mail addresses: claudio.mazzotti@unibo.it (C. Mazzotti), nicola.buratti@unibo.it (N. Buratti).

https://doi.org/10.1016/j.jobe.2021.103176
Received 13 September 2019; Received in revised form 21 August 2021; Accepted 21 August 2021
Available online 6 September 2021

which partially pre-fabricated beams and columns are assembled and completed in order to obtain moment resisting frames, with the cast in-place of the beam column joints, the beam top parts, and the slabs [17–21]. In the following, phase-1 and phase-2 will indicate the states before and after the cast in place, respectively.

The test duration was about two months, at the end of which the beams were loaded up to failure. In the experimental tests, a loading protocol representative of the various construction phases was adopted, in particular, during each phase the loading was kept constant for several days, in order to study the effects of the delayed deformation of the two concretes used for the precast beam and the *in situ* cast. Some cylindrical specimens were also prepared and used for long–term tests, *i.e.*, to evaluate the rheological properties of the concretes and to perform tests at different ages, with measures of strength and stiffness characteristics.

The fibre-based numerical model was applied and validated using the results of the experimental campaign. In particular, the results of the test on the cylindrical specimens were used in order to calibrate the parameter of the rheological models adopted. The so calibrated model was then used to simulate the behaviour of the two beams under long-term serviceability loads. The model showed good accuracy in the prediction of the experimental moment-curvature diagrams, of the beams deflection, and also of the strains in the rebars.

2. The numerical model

The evaluation of the long-term deflection of a structural element under flexure requires the consider different issues at different scales: the material behaviour (creep of concrete), the cross-section behaviour (interaction with steel reinforcement), and the structural behaviour (presence of cracks).

In the following, each aspect is considered and introduced, leading to the proposed numerical model.

2.1. The creep model

In order to evaluate the long-term behaviour of concrete under variable stresses over time without solving a convolution problem, the viscoelastic model for the creep of concrete in compression is written following the incremental form [10]:

$$\dot{\sigma} = E_{eff}\dot{\varepsilon}^{el}, \tag{1}$$

where $\dot{\varepsilon}^{el}$ is the elastic strain rate and E_{eff} is the effective modulus which increases over time because of concrete ageing. The total strain rate is defined as the sum of two different contributions:

$$\dot{\varepsilon} = \dot{\varepsilon}^{el} + \dot{\varepsilon}^{v} \tag{2}$$

where $\dot{\varepsilon}^{v}$ is the viscous strain rate. The strain splitting assumption (2) is adopted in several formulations in the framework of infinitesimal deformations [10,22]. Combining Eq. (1) and Eq. (2) it is possible to write:

$$\dot{\sigma} = E_{eff}(\dot{\varepsilon} - \dot{\varepsilon}^{v}). \tag{3}$$

The stress rate $\dot{\sigma}$ is now defined making use of a modified version of the solidification theory [10]. According to this theory, originally proposed by Bažant [9] for linear viscoelasticity, the age-dependent behaviour of concrete is described by threating the solidifying material (the hydrating cement paste in this case) as a varying composite, the components of which are characterized by age-independent mechanical properties. The ageing process is modelled as a change of concentration of solidified matter, whose volume is described by a function $\nu(t)$, with $0 < \nu(t) \leq 1$[23,24]. This simple mechanical model aims at describing, empirically, many different physical/chemical phenomena occurring during concrete ageing; the growth of mass of the cement hydration products per unit volume being the main physical mechanism. In addition, during concrete hardening, the relaxation of localized high stress concentrations in the microstructure of the cement gel also occurs, as described by the microprestress-solidification theory [25,26]. This phenomenon is not considered in the present formulation.

According to the solidification theory, the subsequent deposited layers of solidified constituent are assumed to be coupled in parallel and subject to the same macroscopic strain increment dε, when contributing in equilibrating the compressive stress. The layers of cement gel already solidified carry a finite stress s, while those not yet solidified are assumed stress free ($s = 0$).

The solidifying constituent is considered as a non-ageing viscoelastic material characterized by the micro-relaxation function $\Psi(\xi)$, where $\xi = t - t'$, being t' the time at which the load is applied. Indicating by $\nu(\tau)$ the volume of solidified matter at the general time τ, the stress s at age $t > \tau$ in the solidifying layer $d\nu(t)$ is:

$$s(\tau, t) = \int_{\tau}^{t} \Psi(t - t')d\varepsilon(t') \tag{4}$$

where the limits of integration reflect the assumption that a layer is stress free prior to solidification, i.e. before the time τ. Making use of Eq. (4), it is possible to write an equilibrium equation between the macroscopic stress σ and the micro stresses $s[\nu(t)]$ at general layers as:

$$\sigma(t) = \int_{t'=0}^{t} \Psi(t - t')\nu(t')d\varepsilon(t') \tag{5}$$

Then, the relaxation function, $R(t,t')$, is the product of two functions: the function $\nu(t')$ depending on the concrete age at the time of loading t', and the function $\Psi(t-t')$ depending on load duration, $t - t'$:

$$R(t, t') = \Psi(t - t')\nu(t') \tag{6}$$

Adopting a Dirichlet series expansion for the micro-relaxation function $\Psi(t-t')$ [27]:

$$\Psi(t - t') = E \cdot e^{-(t-t')/\tau} \tag{7}$$

Eq. (5) can be rewritten in differential form as:

$$\dot{\sigma}(t) + \frac{\sigma(t)}{\tau} = E \cdot \nu(t) \cdot \dot{\varepsilon}(t) \tag{8}$$

corresponding to the differential equation governing a Maxwell unit with ageing modulus $E(t) = \nu(t) \cdot E$ and constant dashpot viscosity $\eta = \tau E$, where τ is the characteristic relaxation time.

Bazant and Prasannan [23,24] proposed a more general solidification theory based on n different solidification processes characterized by different volume increments $d\nu_{\mu}(t')$ $(\mu = 1,\ldots,n)$. Under this assumption the following system of first-order differential equations is obtained:

$$\begin{cases} \sigma(t) = \sum_{\mu=1}^{n} \sigma_{\mu}(t) \\ \dot{\sigma}_{\mu}(t) + \dfrac{\sigma_{\mu}(t)}{\tau_{\mu}} = E_{\mu} \cdot \nu_{\mu}(t) \cdot \dot{\varepsilon}(t) \quad \mu = 1, \ldots, n \end{cases} \tag{9}$$

corresponding to and ageing Maxwell chain of n units with n constant relaxation times τ_{μ}. For a general Maxwell chain the identification problem of a set of elastic ageing moduli $E_{\mu}(t) = E_{\mu}\nu_{\mu}(t)$ is ill conditioned [23,24], because of the high deviation and the very short observation time of experimental data normally available. Therefore, it is preferable to adopt at most two different solidification functions: $\nu_1(t)$ and $\nu_n(t)$. The former describes the ageing of the first n – 1 Mx units and the latter modulates the last unit.

In the present model the last unit is a degenerated unit consisting of an elastic spring of modulus $\nu_n(t)E_n$ in order to ensure an asymptotic creep strain.

Starting from Eq. (9) the stress rate can be expressed in the following form:

$$\dot{\sigma}(t) = \sum_{\mu=1}^{n} \dot{\sigma}_\mu(t) = \sum_{\mu=1}^{n} E_\mu \cdot \nu_\mu(t) \cdot \left[\dot{\varepsilon}(t) - \frac{\sigma_\mu(t)}{E_\mu \cdot \nu_\mu(t) \cdot \tau_\mu} \right] \tag{10}$$

It is worthy noticed that, being based on an incremental formulation, the solidification theory does not require storage of the whole stress history.

2.2. Incremental formulation of the creep model

As previously discussed, a rate-type formulation of the creep problem is convenient because it does not require the solution of a convolution problem. In the present study a modified version of the exponential algorithm, originally proposed by Zienkiewicz and Watson [28], and Bažant and Wu [29], and already presented in Mazzotti and Savoia [10], is adopted.

This model admits time steps of variable amplitude without numerical stability problems [10], because it is based on the integration of Eq. (10) over the time step, under particular assumptions. The key idea of the exponential algorithm is to integrate the differential Eq. (10) exactly, under the assumption that quantities independent form the stress are constant over the time step. In particular, the interval of time under consideration is divided into N time intervals $\Delta t_r = t_r - t_{r-1}$ $(r = 1, \ldots, N)$.

Multiplying Eq. (9) by the integration function:

$$f_\mu(t) = e^{\int_{t_{r-1}}^{t} \frac{dt'}{\tau_\mu}} \tag{11}$$

it is possible to write:

$$\frac{\partial}{\partial t} \left[\sigma_\mu(t) e^{f_\mu(t)} \right] = E_\mu \nu_\mu(t) \dot{\varepsilon}(t) e^{f_\mu(t)} \tag{12}$$

Integrating Eq. (12) over the general time step, the following expression is obtained:

$$\sigma_\mu(t_r) = e^{-f_\mu(t_r)} \left[\sigma_{\mu,r-1} + \int_{t_{r-1}}^{t_r} E_\mu \nu_\mu(t') e^{-f_\mu(t_r)} d\varepsilon(t') \right] \tag{13}$$

where $\sigma_{\mu,r-1}$ indicates the value of the state variable at the step r-1. The parameters at the right member of Eq. (13) can be assumed constant either when the time steps are sufficiently small or when there are small variations of the ageing functions $\nu_\mu(t)$. In this case, setting $t = t_r$, the following relationship is obtained:

$$\sigma_{\mu,r}(t) = \sigma_{\mu,r-1} e^{-\frac{\Delta t_r}{\tau_\mu}} + E_\mu \nu_{\mu,r-1/2} \cdot \lambda_{\mu,r} \Delta \varepsilon_r \tag{14}$$

where:

$$\lambda_{\mu,r} = \left(1 - e^{-\frac{\Delta t}{\tau}} \right) \frac{\tau_\mu}{\Delta t_r} \tag{15}$$

and

$$\nu_{\mu,r-1/2} = \frac{1}{2} \left(\nu_{\mu,r-1} + \nu_{\mu,r} \right) \tag{16}$$

Combining Eq. (14) and Eq. (9) it is finally possible to derive an incremental pseudo-elastic formulation:

$$\Delta \varepsilon_r = \frac{1}{E''_r} \Delta \sigma_r + \Delta \varepsilon''_r \tag{17}$$

where

$$E''_r = \sum_{\mu=1}^{N} \lambda_{\mu,r} \cdot E_\mu \cdot \nu_{\mu,r-1/2} \tag{18}$$

and

$$\Delta \varepsilon''_r = \frac{1}{E''_r} \sum_{\mu=1}^{N} \left(1 - e^{-\frac{\Delta t_r}{\tau_\mu}} \right) \sigma_{\mu,r-1} \tag{19}$$

This formulation, allowing the usage of variable time steps, is computationally efficient and preserves accuracy and stability. Further details are available in Mazzotti and Savoia [10].

2.3. Cross-section fibre model

The viscoelastic model of concrete described in the previous Section has been implemented in a cross-section fibre model for RC members. For given axial loads and bending moments applied to the cross-section at a given time, the stress-strain distributions in the concrete and in the rebar are obtained by the two-step iterative procedure described in the following.

The cross section is first divided into a number of layers, named fibres (see Fig. 1). The assumption of plain strain profile is also introduced. For a prescribed value of curvature, an initial trial position of neutral axis is set; accordingly, a strain profile is assumed. For each fibre, using the proper constitutive relationships, the stresses are calculated. The internal resultant axial force, N, is then compared with the external applied load; if the equilibrium condition is not fulfilled, a new neutral axis position will be chosen maintaining the same curvature $\Phi = 1/\rho$, where ρ is the radius of curvature. The iterative procedure stops when the internal axial force equals the external axial force.

The value of bending moment can now be evaluated from the stress distribution over the cross section and compared with the corresponding prescribed external bending moment. If the difference between the two values exceeds a given tolerance, the curvature is increased and the whole procedure starts again. According to this procedure when a constant external bending moment is applied, the curvature increases over time because of the viscosity term in Equation (8). In the end, the two-steps iterative procedure leads to the curvature evolution with time given a general history of external bending moment and axial force applied to the general cross-section.

2.4. Effect of shrinkage

Concrete not only exhibits long-term deformations due to loads (creep strain), but also shows load-independent deformations over time (shrinkage strains). This second contribution has been also introduced into the material model described in Section 2.1 by adding the corresponding shrinkage strain rate, $\dot{\varepsilon}^s$, to Eq. (2):

$$\dot{\varepsilon} = \dot{\varepsilon}^{el} + \dot{\varepsilon}^{v} + \dot{\varepsilon}^{s} \tag{20}$$

In real applications, the percentage of shrinkage strain occurring before the beginning of the long-term tests produces self-balanced internal stresses inside the general cross-section since the steel rebars are perfectly bonded to the concrete and they can be considered as made of a perfectly elastic material (at least under serviceability conditions). This self-equilibrated stress distribution over the cross-section may reduce the external bending moment required to produce cracking, and therefore must be taken into account in the numerical model. To do so, the procedure proposed by Ghali and Favre [4] was used in the present work. In particular, the bending moment increment due to this early shrinkage was estimated as

$$\Delta M_{sh} = \varepsilon_{sh} \cdot B \cdot \frac{E_c}{1 + \chi \varphi} \tag{21}$$

where ε_{sh} is the shrinkage strain occurred before the beginning of the tests, B is the section modulus of the steel bars only, E_c is the concrete elastic modulus, χ is the ageing coefficient and φ is the creep coefficient.

Finally, it is worth noticing that shrinkage in the early days also affects the tension stiffening model, in fact it shifts the moment curvature

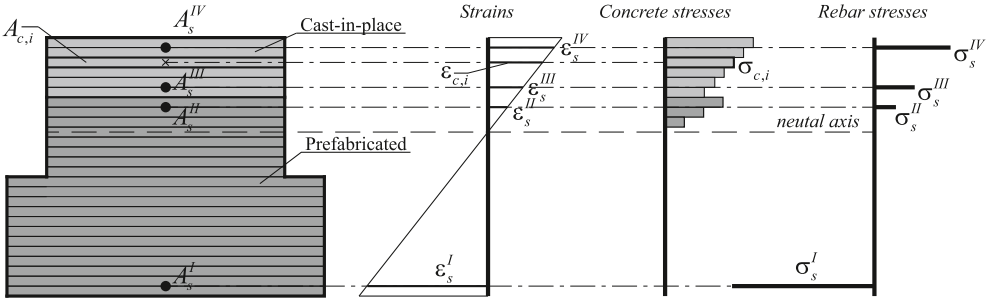

Fig. 1. Fibre-based model adopted in the present paper.

diagram by $\Delta\Phi_{cs} = 1/\rho_{2,sh}$ which can be evaluated as [30]:

$$\frac{1}{\rho_{2,sh}} = k_{cs2}\frac{|\varepsilon_{sh}|}{d} \tag{22}$$

where d is the cross section effective depth, and k_{cs2} is a function of the reinforcement ratio and of the ratio of the steel elastic modulus over the concrete modulus. These specific effects of early shrinkage will be applied later to the case studies. The shrinkage gradient between the core and the surface of cross sections was not considered, as in typical design approaches.

2.5. Tension stiffening

Moving from the cross-section to the entire element, cracking has to be taken into account. In this perspective, the local curvature value has been modified in order to introduce the tension stiffening effect and thus becoming a mean curvature value. This effect has been considered in the numerical model according to the formulation proposed by the Model Code 2010 [3]. In particular, the average curvature of a cross section can be evaluated as:

$$\Phi_m = \gamma \cdot \Phi_{uc} + (1-\gamma)\Phi_c \tag{23}$$

where Φ_{uc} and Φ_c are the un-cracked and fully cracked curvatures, respectively. The coefficient γ is defined as:

$$\gamma = \left(\frac{M_{cr}}{M}\right)^{\alpha} \tag{24}$$

where M_{cr} is the cracking bending moment, M is the applied bending moment, and α is a parameter that is assumed equal to 2 in the present paper [3].

When considering beams cast in different phases, it is important to notice that the cracking bending moment changes from phase-1 to phase-2, because of the cross-section enlargement. Therefore, the cross section may crack in phase-1 and remain cracked even if the bending moment in phase-2 is smaller than the corresponding cracking bending moment. For this reason, the simple model in Eq. (23) has been modified considering incremental approach for the behaviour in phase-2:

$$\begin{cases} \Phi_m(t_i) = \Phi_{uc}(t_i)\gamma_1 + \Phi_c(t_i)(1-\gamma_1) \ \text{ in phase } 1 \\ \Phi_m(t_i) = \Phi_m(t_{i-1}) + [\Phi_{uc}(t_i) - \Phi_{uc}(t_{i-1})]\gamma_2 + \\ \quad + [\Phi_c(t_i) - \Phi_c(t_{i-1})](1-\gamma_2) \ \text{ in phase } 2 \end{cases} \tag{25}$$

where γ_1 and γ_2 indicate the values of the tension stiffening coefficient in phase-1 and phase-2, respectively. A different cracking moment was used for the calculation of γ_1 and γ_2, i.e. the cracking moment for the phase-1 cross section in the first case and the cracking moment for the phase-2 cross section in the second.

Once the curvature diagram is defined, the deflection at mid-span can be computed using the general formula:

$$\delta = \int_0^{l/2} \Phi(x)\cdot x \cdot dx \tag{26}$$

where x indicates the distance from one of the supports and l the total length of the beam. In the present study the mid-point integration rule was used to solve Eq. (26). In particular the beam was divided into an even number, N_s, of segments and for each of them the average curvature was computed considering the tension stiffening model in Eq. (25). Taking advantage of the symmetry of the problem, the mid-span deflection at time t_i was computed as:

$$\delta(t_i) = \sum_{j=1}^{N_s/2} \Phi_m^j(t_i)\Delta z_j^2 \tag{27}$$

where $\Phi_m^j(t_i)$ and Δz_j are the average curvature and the length of the segment j, respectively. This procedure can be used only when dealing with statically determined structural elements. The definition of the deflection of statically redundant cracked elements under long-term loads is out of the scope of the present paper.

3. The experimental campaign

3.1. Overview

3.2. The beams tested

Both beams tested were 9350 mm long, but had different cross sections (Fig. 2 and Fig. 3). The first beam, beam-1 in the following, had an overall 800 × 750 mm (width x height) cross section while the second beam, beam-2 in the following, had an overall 800 × 650 (width x height) mm cross section (Fig. 3). In particular, the cross sections of beam-1 at mid-span and at the supports are reported in Fig. 3a. In Phase 1, the precast concrete cross-section is 550 mm deep, whereas after the *in situ* cast the depth increases to 750 mm. In the two end portions of the beam the precast cross-section is hollow, in order to allow the placing of the steel rebars necessary to resist the hogging bending moment and to allow a more effective detailing of beam–column nodes in multi–storey structures. The cross-sections of the Beam-2 are reported in Fig. 3d–f. Its general their features are similar to Beam-1, the main differences being the cross section depth and the number of steel bars. The cross-section sizes of the two beams considered are among the most widely used in the construction system considered. The longitudinal arrangement of the steel reinforcement for the two beams is reported in Fig. 2, with a simplified indication also of the positions of instruments. Fig. 3 shows with more detail the transverse steel reinforcement which is composed by a truss system with vertical and inclined bars in the central portion of the beam and by stirrups in the lateral portions. The difference between beams being the overall height and the position of some instruments.

3.3. Experimental set-up

The beams were loaded using a four-point scheme, by means of two hydraulic jacks that were supported by two reaction frames connected to

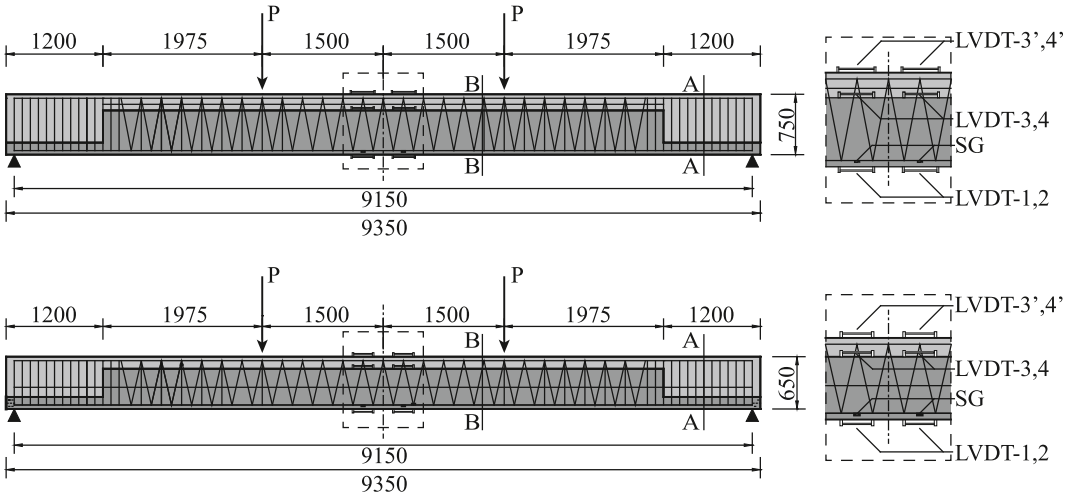

Fig. 2. Longitudinal sections of beam-1 (a) and beam-2 (b) showing the layout of the rebars and the positions of the LVDT and strain gages (SG) used in the present work as reference for the numerical model. The pre-fabricated parts of the beam are in dark grey and the cast-in-place parts in light grey. Length units are mm.

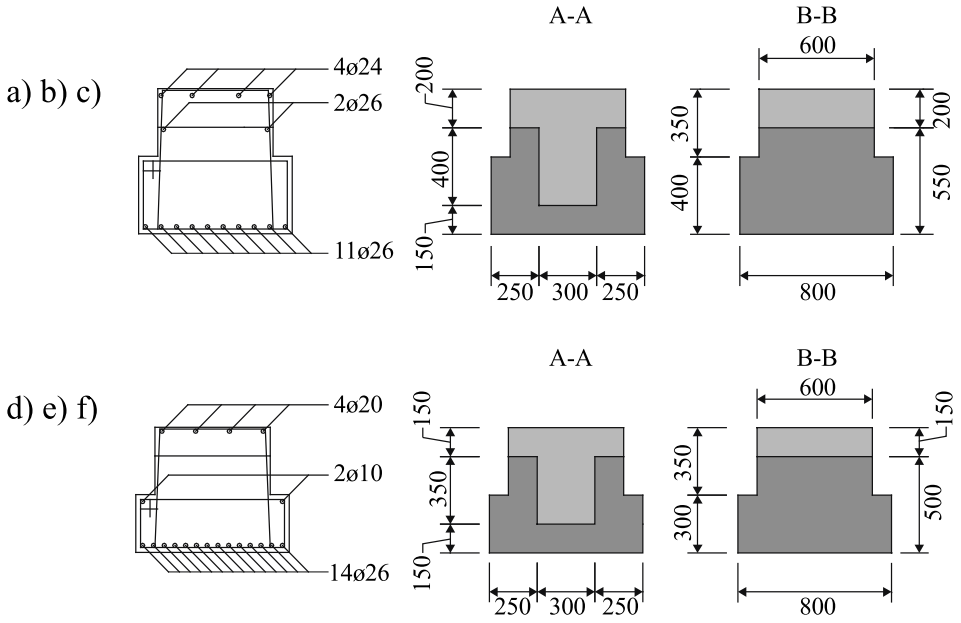

Fig. 3. Cross-sections of beam-1 (a, b, c) and beam-2 (d, e, f). Figures (a) and (d) illustrate the longitudinal reinforcement in the central portion of the beam. Figures (b) and (e) illustrate the pre-fabricated (dark grey) and the cast-in-place (light grey) parts in the central portion of the beams (cross-section B-B in Fig. 2) while Figures (c) and (f) illustrate the pre-fabricated (dark grey) and the cast-in-place (light grey) parts at the supports (cross-section A-A in Fig. 2). Length units are mm.

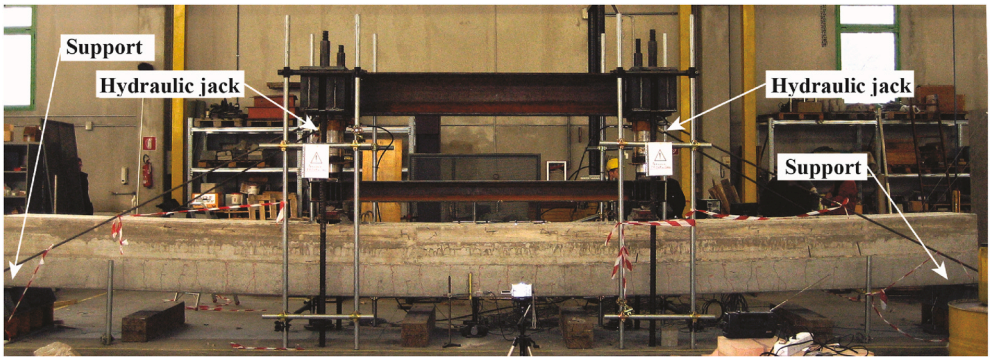

Fig. 4. Beam-2 during the failure test.

the strong floor of the laboratory (see Fig. 4). A specific hydraulic system was used able to keep the load level constant with time; tests were performed under load control.

Fig. 2 shows some of the sensors adopted during the long-term tests, i.e. only those used in the present paper as reference for the numerical model. Two horizontal LVDTs were placed, on each cross-section, at the upper and lower faces of the beam; the horizontal distance between the centres of the two LVDTs is 50 cm. The LVDTs on the upper face of the precast beams (LVDT-3,4 in Fig. 2) were removed before casting of phase 2 and subsequently moved on the new upper face, after the hardening of the new cast in-situ concrete (LVDT-3′,4' in Fig. 2). Five LVDTs in the vertical direction –not indicated in the figures– were placed along the beam to measure deflections of the bearing supports, of loading points and at mid-span. Strain gages were glued to the steel bars in the tensile and compression zone.

3.4. Loading protocol

In order to reproduce the construction phases of the beams, loads were applied and maintained constant during various time intervals. Fig. 5a shows the sequence of the loading steps for the beam-1. Force P is intended as the one applied by each hydraulic jack.

The precast part of beam-1 was transported to the Structural Testing Laboratory 19 days after casting, lifted-up and placed in the testing configuration. At this stage the only load on the beam was its own self-weight (not included in Fig. 5a); during this procedure the strains were monitored. The stresses due to self-weight were small (M = 110 kNm at mid-span), and no cracks in the beam were visible. The corresponding strains were about 50 με in the concrete in compression and 40 με in the tensile steel bars. This loading phase is not reported in the diagrams showed in the following sections. Subsequently, a force increment ΔP = 127 kN was applied by using the hydraulic jacks in order to obtain a bending moment at mid-span corresponding to the one theoretically produced by the weight of all the precast slab elements, which are simply supported by the beam. Due to some technical reasons, in this first phase the weight of the concrete cast to complete the slabs in the prefabrication system under consideration was also applied, even if theoretically this is not completely consistent with real construction process. In fact, only after further 7 days the beam was completed with the in-situ cast. Therefore, the load increment indicated in Fig. 5a at day 26 refers only to the force equivalent to the weight of the real cast in place concrete used to complete the beam, that would produce the same bending moment at mid-span. After 27 days under these loads a further load increment (phase-2 load), ΔP = 50 kN, was applied, corresponding to the effect of all permanent loads and of a fraction (30%) of the variable loads. This level of loading corresponds to the quasi-permanent load combination. After further 17 days under constant load, the beam was loaded up to failure.

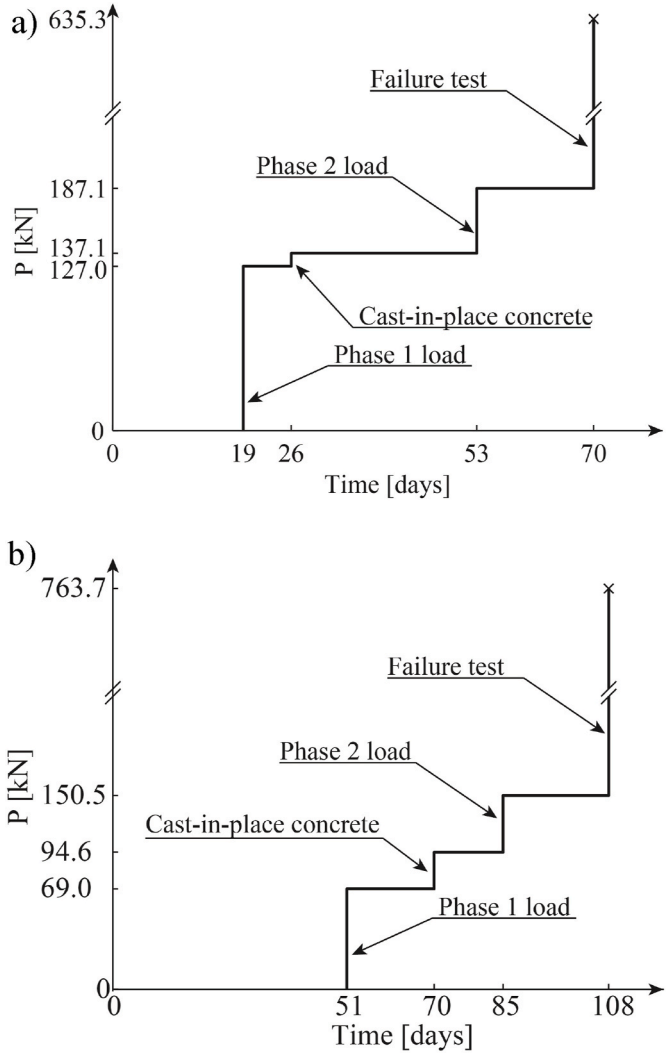

Fig. 5. Loading protocol for beam-1(a) and beam-2 (b). The origin of the time axis corresponds to the cast of the prefabricated portion of the beams.

The loading protocol for the beam-2 was similar but not identical, and is depicted in Fig. 5b. In this case, the test started 51 days after the cast of the precast part of the beam. The phase 1 load, 69.0 kN, corresponds to the weight of all the precast slab elements. The force was increased to 94.6 kN 19 days after the beginning of the tests, in order to simulate the weight of the cast-in-place concrete –used to complete the slabs. The phase-2 increment, ΔP = 55.9 kN, was applied 34 days after the beginning of the test and kept constant for 23 days. Finally, 57 days after the beginning of the test the beam-2 was loaded up to failure.

The load values adopted were derived from case study structures, used as multi-storey car-parking. In fact, these latter are a kind of structure in which the building technology under investigation is most commonly used.

3.5. Material properties

3.5.1. Short-term properties. Table 1 shows the mix design of the concretes used to build the precast beams (Phase-1) and the completion of the cross-section (Phase-2). Values of strength and elastic modulus obtained for the two concretes are reported, as a function of the number of days from casting, in Table 2 and Table 3 for beam-1 and beam-2, respectively. Concerning cast in place concrete for beam-1 34 days are the age at the time of phase-2 loading, while 51 represent that at the time of the failure test. As for beam-2 3 days are earliest age at which the cast in place concrete could be tested, while 38 days are its age at the time of the failure test. The strength and stiffness characteristics were obtained from compression tests at different times on cylindrical specimens obtained from the same concrete batches used to realize each

Table 1
Concrete admixtures used for the two beams.

Component	Unit	Phase-1 concrete		Phase-2 concrete	
		Beam-1	Beam-2	Beam-1	Beam-2
Cement 52.5 R	kg/m^3	380	377	-	
Cement 32.5	kg/m^3	-	-	405	391
Filler Plastofill HSC	kg/m^3	19.5	3	-	
Sand (fine)	kg/m^3	933	864	845	135
Sand (gross)	kg/m^3	-			569
Gravel 6–12 mm	kg/m^3	910	898	-	-
Gravel 5–15 mm	kg/m^3	-		925	627
Gravel 12–20 mm	kg/m^3	-			450
Water	l/m^3	150	177	195	199
Superplasticizer	l/m^3	2.8	3.01	4.13	4.59

Table 2
Mechanical properties of the concretes of beam-1 at different ages.

	Unit	Concrete for prefabrication			Cast-in-place concrete	
Age	Days	19	53	70	34	51
f_{cm}	MPa	51	58	59	30	32
E	MPa	36022	-	39017	26545	26029

Table 3
Mechanical properties of the concretes of beam-2 at different ages.

	Unit	Concrete for prefabrication			Cast-in-place concrete	
Age	Days	51	70	108	3	38
f_{cm}	MPa	66	67	68	14	25
E	MPa	32600	34016	38012	17520	24250

beam tested. The tests have been conducted at the times of application of the loads to the beam or at the time of realization of the completion cast of the beams. The mean yielding stress of the steel bars, obtained from tensile tests on samples extracted from the rebars, is $f_{ym} = 490$ MPa. The rebars used in the two beams were from the same batch therefore no significant differences were observed in their yielding strengths.

3.5.2. Long-term properties. Cylindrical specimens were used to measure the shrinkage and creep strains of the considered concretes. The creep tests started at the same time of loading of the beams. A loading protocol as similar as possible to that of the concretes in the compression zone of the beams was adopted. Fig. 6a shows the instantaneous creep (C) and shrinkage (S) strains development over time for the concretes used for the beam-1. The shrinkage strain measurement on the precast concrete started at the same time of first loading while on the cast-in-place concrete shrinkage strains were measured starting from 5 days after casting; in this way, the first part of the shrinkage (from hardening to 5 days) was not measured. As for the creep behaviour, on the precast concrete (I) an initial stress equal to 12.9 MPa was applied 19 days after casting and was increased to 14.5 MPa after 33 days. For the cast-in-place concrete (II), the initial applied stress was 3.2 MPa and the test started 33 days after the first loading. The delay between the real casting of the concrete and the starting of the creep test was due to technical problems but did not affected (as will be described in the following) the validity of the test. Fig. 6b shows the delayed deformations measured on the cylindrical specimens cast using the concretes used form the beam-2. In this case a stress equal to 6.9 MPa was applied 51 days after casting and increased by 4.0 MPa after 19 days in order to simulate the effect of the weight of the cast-in-place concrete. The stress was increased by 2.3 MPa after further 15 days to simulate the phase-2 loads. The test of the cast-in-place concrete started with a stress equal to 3.5 MPa which was applied three days after casting and was increased by 2.6 MPa after 12 days to simulate the effect of phase-2 loads.

3.6. Test results

The following sections will describe the behaviour of the two beams tested. Corresponding results will be presented independently because dimensions of the beams cross-sections and applied forces are different and therefore a direct comparison would not be meaningful. Not all the available results will be presented here, but only those that will be compared with the predictions coming from the described numerical model in the next Section.

3.6.1. Beam-1. This Section describes the instantaneous and long-term behaviour of beam-1 in terms of force – mid-span deflections. Further details on the delayed strains of concrete and steel rebars measured during the test are available elsewhere [21].

Fig. 7 shows the applied force P versus the mid–span deflection and the evolution over time of the mid–span deflection, respectively. In

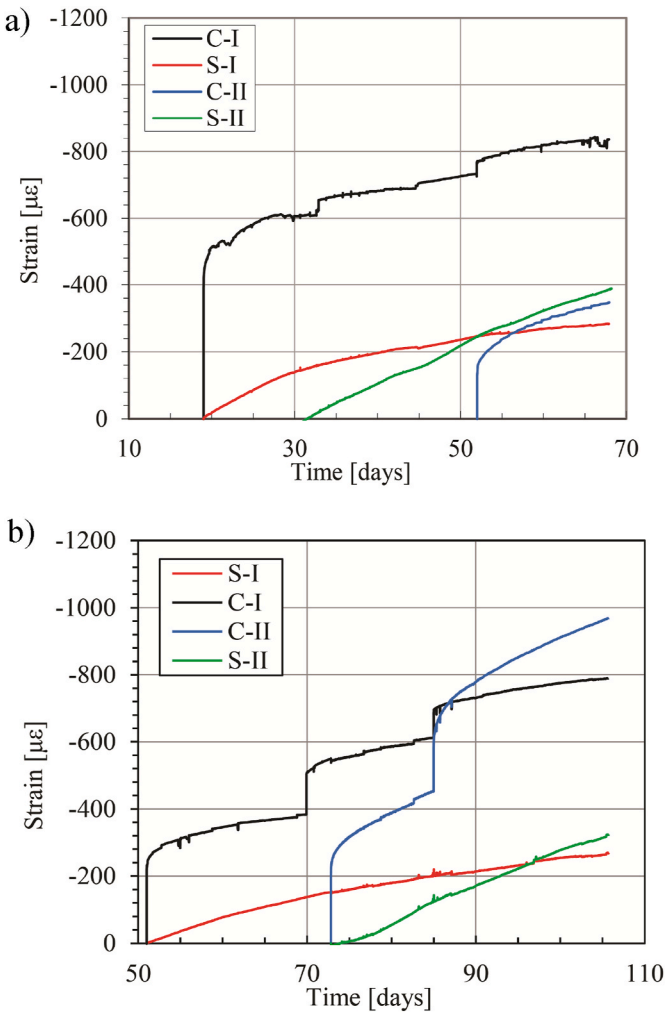

Fig. 6. Shrinkage (S) and compression creep strains (C) measured on the cylindrical specimens of the concretes used for the prefabrication (I) and the cast-in-place (II) of beam-1 (a) and beam-2 (b).

particular, from Fig. 7a the applied loading sequence can be observed until final failure, performed at the end of the long-term loading. In this figure, horizontal lines indicate deflection increases under constant loads. In the first part of the curve the tension–stiffening effect may also be noticed. The stiffness increase for $P > 127$ kN is due to the completion of the beam with the cast–in place concrete.

Approaching failure, the last part of the curve, a non–linear behaviour can be noticed. The tensile rebars yielded at about 600 kN and the post yielding branch of the curve led to the concrete compression failure that was observed for $P = 640$ kN.

The evolution of the deflection with time, reported in Fig. 7b, shows the behaviour of the beam under serviceability conditions (see Fig. 5a for the loading protocol). It is worth noticing that at the early stages after casting of the cast–in situ concrete, an increase of the delayed deflection rate was observed, due to the increase of load without a corresponding increase of mechanical properties (concrete very young). Subsequently, when the concrete gained mechanical strength and stiffness and the beam cross section progressively reached its final configuration, the deflection rate became steady.

3.6.2. Beam-2. Fig. 8a–b shows the applied force P versus the mid–span deflection and the evolution with time of the mid–span deflection, respectively. Similarly to what discussed for beam-1, the long-terms test was carried out by applying the loading increments indicated in Fig. 5b, and was completed by loading until failure.

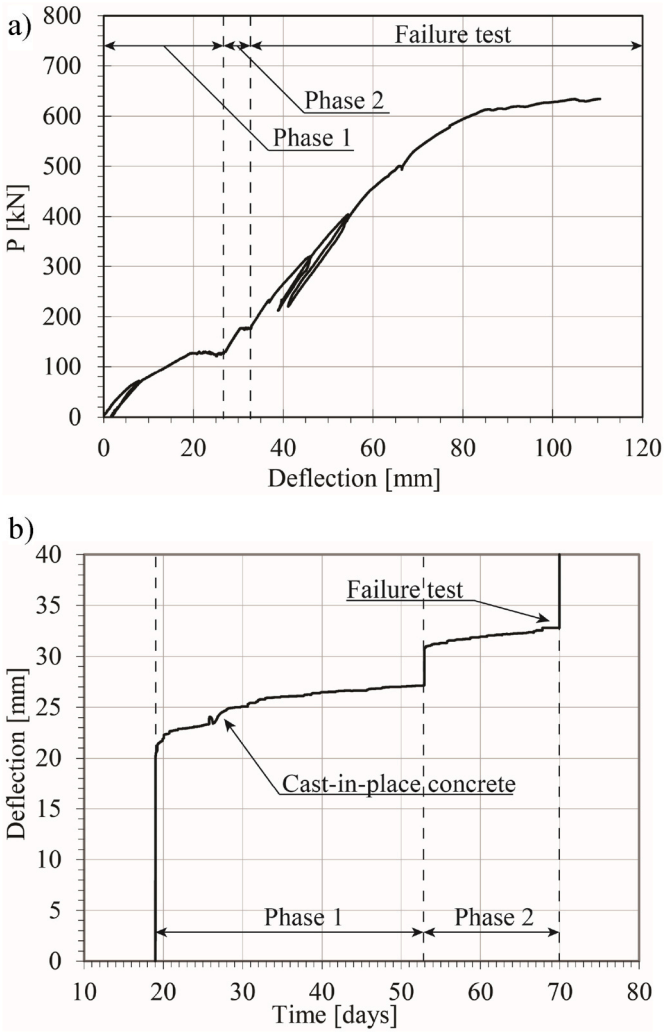

Fig. 7. Beam-1: load-deflection curve (a) and development over time of the deflection (b).

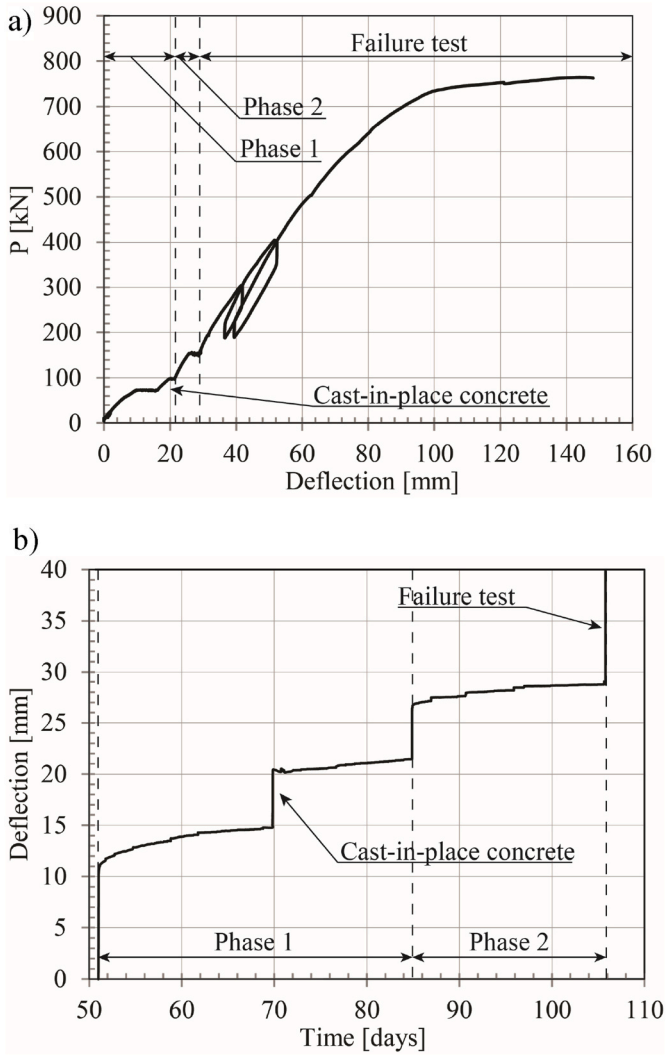

Fig. 8. Beam-2: load-deflection curve (a) and development over time of the deflection (b).

In particular, from Fig. 8a the stiffness increase due to the ageing of the cast-in-place concrete is clearly visible. The first cracks opened during the application of the phase-1 load. During the failure test the tensile rebar yielded at about 740 kN and the beam showed a limited hardening behaviour. Failure (760 kN), as previous case, was due to concrete crushing.

Fig. 8b shows that delayed deflection rate after each load increment decreases due to both the concrete ageing and the cross-section completion.

4. Calibration of the rheological models

This section describes the calibration process of the rheological models, introduced in Section 2.2, that were used in order to simulate the long-term experimental behaviour of the concrete of the beams.

4.1. Shrinkage

The shrinkage of the concretes used in the tests was described using a model similar to the one proposed by Model Code 2010 [3]:

$$\varepsilon_s(t) = C_0 \left(\frac{t}{C_1 + t} \right)^{C_2} \tag{28}$$

whose unknown regression parameters, C_0, C_1, and C_2, were determined by least square regression starting from the shrinkage strains measured from the cylindrical specimens described in Section 3.5.2.

4.2. Relaxation functions

The model described in Section 2.2 requires the definition of the micro relaxation functions Ψ_μ for the concretes adopted and therefore the definition of the pseudo elastic parameters E_μ, τ_μ, and of the ageing functions ν_μ. The strain measured on the cylindrical specimens tested for compression creep and described in Section 3.5.2 were used to this purpose. It is worth noticing that the creep tests were characterized by some discrete stress increments, in order to investigate the ageing effects also. In fact, since the stress increments were applied at different times, it is possible to derive from a single test multiple creep curves, after isolating the deformations produced by each stress increment. Calibration of the ageing functions, together with the pseudo elastic coefficients, becomes straightforward.

4.2.1. Definition of the creep curves for each stress increment

Using the creep curves from the cylindrical specimens the deformations related to the different stress increments were determined as described in the following. Starting from the initial stress application, the first branch of the creep curve (up to the following stress increment) was interpolated using the function:

$$\varepsilon(t) = \varepsilon_0 + \sum_{i=1}^{7} A_i \left(1 - e^{\frac{-t}{\tau_i}}\right) \tag{29}$$

in which ε_0 and A_i are unknown regression coefficients and $\tau = [0.001 \quad 0.01 \quad 0.1 \quad 1 \quad 10 \quad 100 \quad 1000]$, in days. The curve described by Eq. (29) provides a good description of typical creep (see Section 3.5.2). Once calibrated, Eq. (29) was extrapolated and subtracted from the following branch of the creep curve, in order to isolate contributions of the subsequent stress increment. The procedure was repeated for all the stress increments. As an example, the results of the method are illustrated in Fig. 9, with reference to the creep curves coming from the concrete used in the prefabricated part of beam-2.

4.2.2. Definition of the relaxation curves

In order to define the governing parameters of Eq. (9), the most simple way is to consider multiple relaxation problems triggered by unit deformation imposed at different times:

$$\sigma(t, t_0) = \varepsilon(t, t_0) R(t, t_0) \tag{30}$$

In fact, the Maxwell chain described by Eq. (9), has a closed form solution for the relaxation problem which has the form:

$$R(t, t_0) = \sum_{\mu=1}^{N} \nu_\mu(t_0) E_\mu e^{-\frac{(t-t_0)}{\tau_\mu}} \tag{31}$$

This result can be conveniently adopted in order to estimate the pseudo elastic coefficients E_μ starting form experimental data, as described in the following.

The reference relaxation functions, $R(t, t_{0i})$, were defined starting from the individual experimental creep function using the Volterra-type relationship between compliance functions J and relaxation functions R [33]:

$$1 = R(t_0, t_0) J(t, t_0) - \int_{t_0}^{t} J(t, \tau) dR(\tau, t_0) \tag{32}$$

Starting from the experimental compliance functions, $J(t, t_0) = 1 + \varphi(t, t_0)$, based upon the creep coefficient $\varphi(t, t_0)$ computed form creep strains defined in the previous section, Eq. (32) was numerically solved. The so obtained relaxation functions where then interpolated using a model defined as in Eq. (31), setting $N = 7$ and $\tau_\mu = [0.001 \quad 0.01 \quad 0.1 \quad 1 \quad 10 \quad 100 \quad 1000000]$, in days. It is worth noticing that, in this case E_7, being associated to $\tau_\mu = 1000000$, represents a degenerated Maxwell unit and therefore it is the elastic modulus for $t \to \infty$. The interpolation of the relaxation curves is very complex, in fact the variability of the estimates of the parameters is extremely high because of the limited amount of experimental data. In particular, the number of relaxation curves for different loading ages is small and therefore the ageing parameters are extremely uncertain. For this reason only one ageing function, $\nu(t_0)$ was used in the interpolation process. It was defined according to the literature as [33]:

$$\nu(t_0) = \sqrt{e^{s_1\left(1-(28/t_0)^{s_2}\right)}} \tag{33}$$

in which s_1 and s_2 are unknown regression parameters.

The values of the pseudo elastic coefficients obtained from the procedure described above were validated by simulating the compression creep tests on the cylindrical specimens. The model described in Section 2 was used considering a single fibre, describing the behaviour of the cylindrical specimen. Fig. 10 shows a comparison, for concretes of beam 2, between the experimental and the numerical results which confirms the accuracy of the calibration procedure and of the model.

5. Simulation of the experimental results

This section presents a comparison between the results of the numerical model and the test data. Only the behaviour of the beams under serviceability loads will be considered – i.e., excluding the failure test – because the prediction of the beams ultimate bearing loads has already been discussed in Ref. [21] and is out of the capability of the present linear model.

It is worth noticing that the self-weight of the pre-fabricated part of the beam was taken into account in the numerical simulations, in fact this load is not included in the force P reported in Figs. 7 and 8. Therefore, the experimental results were modified in order to take into account the bending moment and the deflection at mid-span produced by the self-weight by considering the uncracked flexural stiffness of the prefabricated part of the beam only.

Table 4 and Table 5 report the values used for the parameters in Eq. (21) and Eq. (22) Those parameters were defined according to the guidelines provided by CEB Bulletin 158-E [30].

The general cross-section was divided in 150 concrete fibres and one single fibre was considered for each specific layer of rebars. Each fibre was characterized by the corresponding constitutive law, as described in the previous sections.

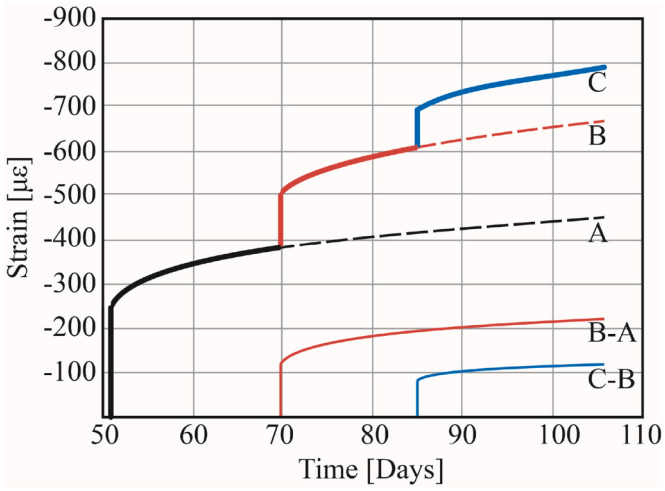

Fig. 9. Interpolation of the experimental creep curves, in order to estimate the creep related to the loads at different ages, for the cylindrical specimens related to the concrete used for the prefabricated part of beam-2.

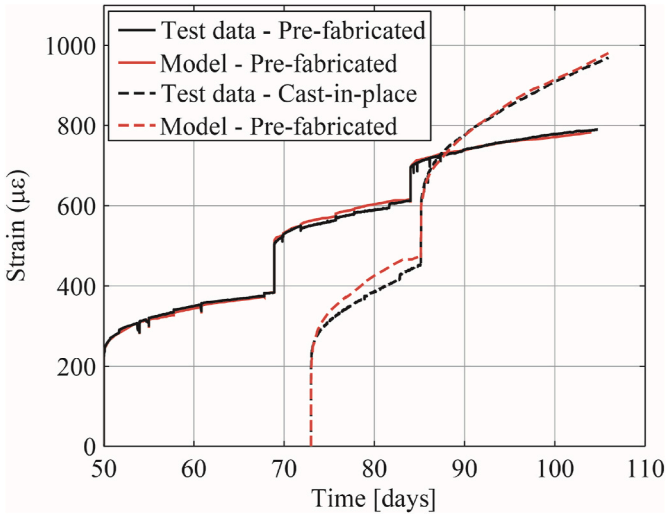

Fig. 10. Comparison of the creep curves predicted by the rheological model with those measured on the cylindrical specimens related to the concretes used for beam-2.

Table 4
Parameters used for estimating the bending moment produced by the shrinkage of the prefabricate part of the beam before the beginning of the 4-point bending test.

	B [mm^3]	E_c [MPa]	ε_{sh} [με]	Φ [−]	χ [−]
Beam-1	0.99 × 106	37520	550	2.5	0.8
Beam-2	1.5 × 106	34016	450	2.5	0.8

Table 5
Parameters used for estimating the curvature increase in the cracked cross section due to the shrinkage deformations developed before the beginning of the 4-point bending test.

	ε_{sh} με	k_{cs2}
Beam-1	450	0.72
Beam-2	550	0.81

5.1. Moment-curvature diagrams

The models described in Section 2 were used in order to simulate the moment-curvature diagrams of the general cross section in the un-cracked and fully-cracked states. At the same time, the experimentally derived moment-curvature curve was computed form the experimental data. In particular the curvatures were calculated using the horizontal LVDTs at the top and at the bottom of the mid-span cross section of the beam (LVDT-1,2 and LVDT-3,4 in Fig. 2).

5.1.1. Comparison with the experimental results

Fig. 11a, shows the numerical moment-curvature diagrams related to the un-cracked (UC), fully-cracked (C) cross sections and to the adopted tension stiffening model (TS) for beam-1, together with the experimental curve. The model is able to simulate with very good accuracy the initial un-cracked behaviour and the onset of cracking but it shows a lower accuracy between 250 kNm and 400 kNm, due to the shape of the tension stiffening curve. The accuracy of the model increases at the end on the phase-1 loading and during the long-term loading phase. In the phase-2 loading, the model tends to overestimate the curvature. In fact, in phase 2 the model predicts a slightly smaller stiffness that the one computed from the experimental results. Fig. 11b shows the time development of the numerical and experimental curvatures. During time also, the accuracy of the prediction is satisfactory, even though some differences can be found mainly due to the instantaneous behaviour.

In Fig. 12a, the comparison between experimental and numerical moment curvature diagrams from beam-2 is reported. In this case the model provides for results in very good agreement with the experimental data, across all the different stages of the tests. The time development of the curvature, plotted in Fig. 12b, is also accurately predicted by the numerical model. The reduced accuracy observed in predicting the moment-curvature diagram for beam-1 (Fig. 11a) is most likely related to the tension stiffening model adopted and to an inaccurate estimation of the tensile strength of concrete over the cross section. In fact, even if the cracking moment is correctly evaluated, right after cracking the numerical moment curvature curve has a more relevant stiffness reduction than the experimental curve, then for a curvature of 2×10^{-6} 1/mm the two curves are consistent, because the beam is fully cracked. Later, after the application of the last load increment the model predicts a stiffness close to the state-2 value, while the experimental curve more similar to the state-1 behaviour.

5.2. Beams deflection

In order to evaluate the long-term load-deflection curve of the considered beams, they were divided into 30 segments at the ends of which curvatures, rotations, and deflections where computed by integrating the curvature diagram with the mid-point rule, starting from the supports. The tension shift effect due to concrete cracking was also included in the simulations for all the cracked segments of the beams. Only the results of the tension stiffening model will be reported in this section.

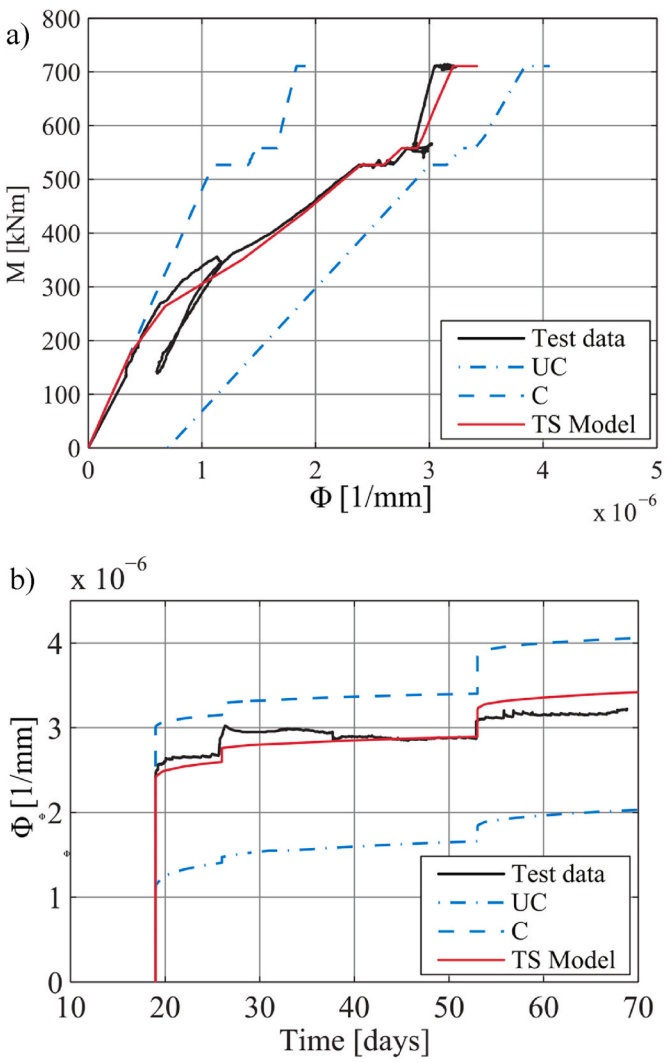

Fig. 11. Beam-1. Comparison between the experimental results, in terms of moment-curvature diagrams, and the results of the numerical simulations for the uncracked (UC) cross section, the fully-cracked cross section (C) and the tension stiffening model (TS).

Fig. 13a shows a comparison between the experimental and the numerical moment vs. mid-span deflection diagrams for beam-1. The model accurately predicts the experimental results at the beginning and at the end of the test but shows a reduced accuracy during the development of the cracking phase; this is due to the strongly non-linear shape of the tension stiffening effect, which cannot be properly followed by the equation adopted in the model. The time development of the mid-span deflection is plotted in Fig. 13b. The model provides a very good prediction of the last part of the test while exhibits a reduced accuracy in the prediction of the early stage of the test. In particular, the largest discrepancy between the two curves can be found after about 26 days since the beginning of the test, the date at which the cast-in-place concrete was cast. Therefore, the lack of accuracy in the prediction most probably arose from the difficulties in modelling the behaviour of the cast-in-place concrete during the first hours/days after casting.

Fig. 14a shows the moment vs. mid span deflection and the mid-span vs. time diagrams for beam-2. In this case the model provides results in

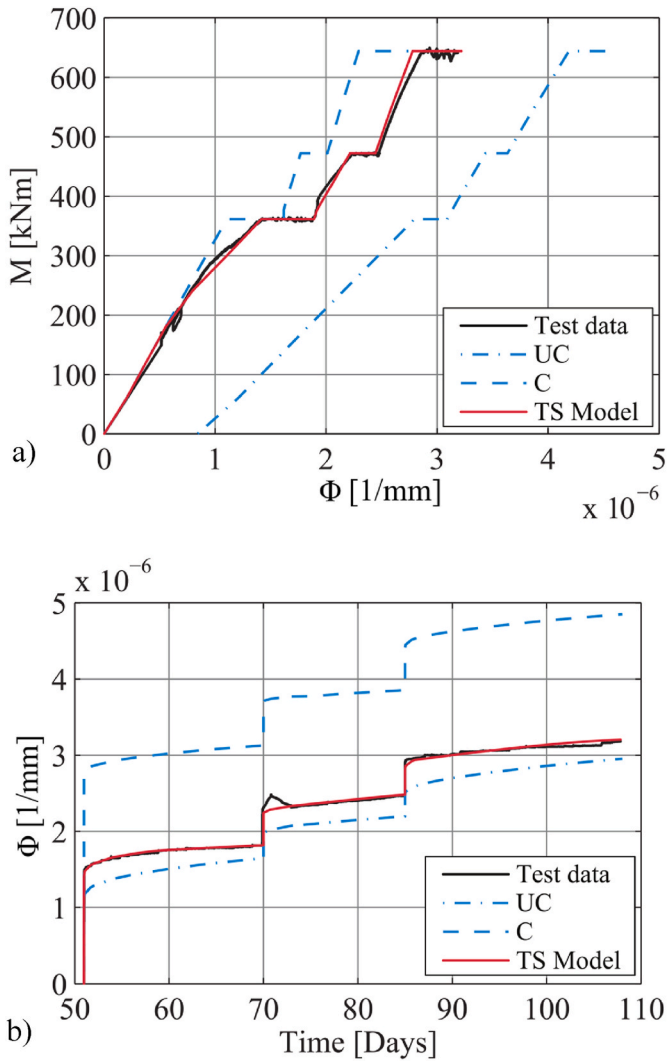

Fig. 12. Beam-2. Comparison between the experimental results, in terms of moment-curvature diagrams, and the results of the numerical simulations for the uncracked (UC) cross section, the fully-cracked cross section (C) and the tension stiffening model (TS).

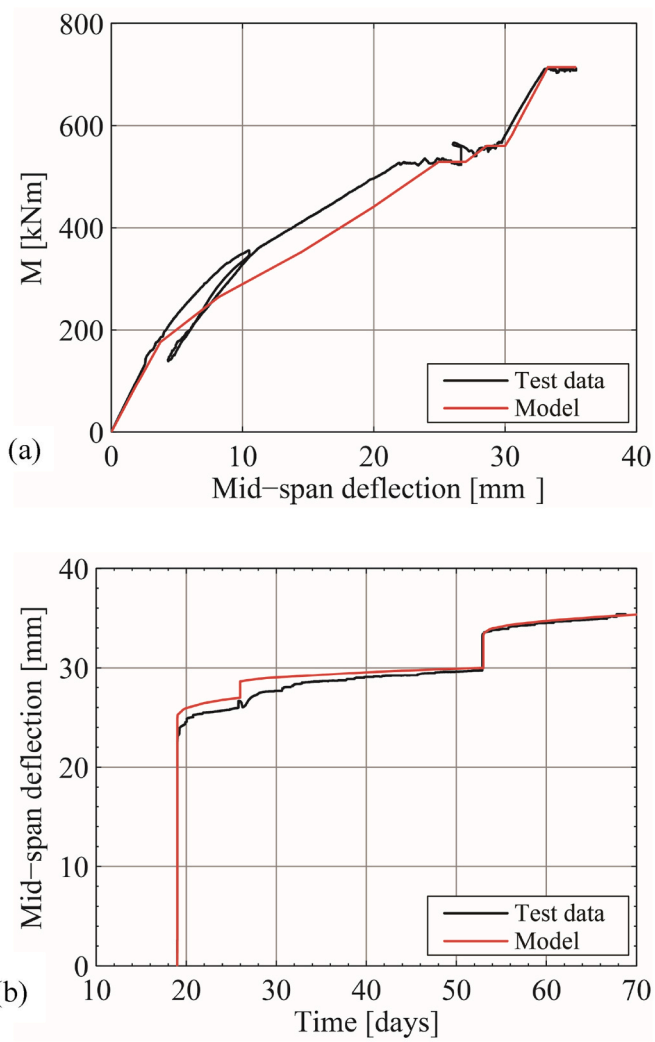

Fig. 13. Comparison between the experimental and the numerical moment vs. mid-span deflection (a) and mid-span deflection vs. time (b) curves for Beam-1.

better agreement with the experimental data with respect to beam-1. In particular, as far as the moment-curvature diagram is concerned, the model shows a very good accuracy across all the different stages of the tests. As noticed for beam-1 the largest difference between the numerical and the experimental curves can be found in the second part of the phase-1 loading.

The time development of the mid-span deflection, plotted in Fig. 14b, confirms the general effectiveness of the prediction of the model.

5.3. Strains

Being the model developed based on a fibre discretization of the cross section, it is very easy to analyse also the time development of the local strains. As an example, the present Section discusses the strain in the tensile rebar at the bottom of the mid-span cross section of the pre-fabricated part of the beam. During the experimental tests these strains were measured using the strain gages indicated in Fig. 2.

Fig. 15 compares the strains predicted by the model for beam-1 (a) and beam-2 (b) with the experimental data. Only results of the tension-stiffening model are reported in the figures. The model shows good accuracy also in this case, in particular regarding beam-1. So far as beam-2 is concerned, the model tends to underestimated the experimental with errors as large as 50 με, which, to the authors, can be acceptable given the complexity of the problem under investigation and the local information considered.

6. Conclusions

The present paper presented a design-oriented numerical model for the simulation of the long-term behaviour of reinforced concrete beams built in different phases. The rheological model adopted for concrete is based on a modified version of the solidification theory and takes into account concrete ageing, shrinkage and creep. This material model was implemented in a fibre based cross section model that allows defining cross sections built in different stages. The model also considers tension-stiffening effects in order to describe concrete cracking.

In the present paper, the model was used in order to simulate the results of experimental tests performed on two RC beams built in two different stages. The parameters of the rheological model were calibrated using data form creep tests in compression. First the model was used in order to simulate the moment curvature relationship of the cross sections of the beams. The numerical simulations provided results in very good agreement with the experimental tests for one of the beams while for the other the accuracy was slightly lower, in particular in terms of prediction of the cracking moment and of the stiffness of the beam after the cast of cast in-place concrete. For both beams, the model

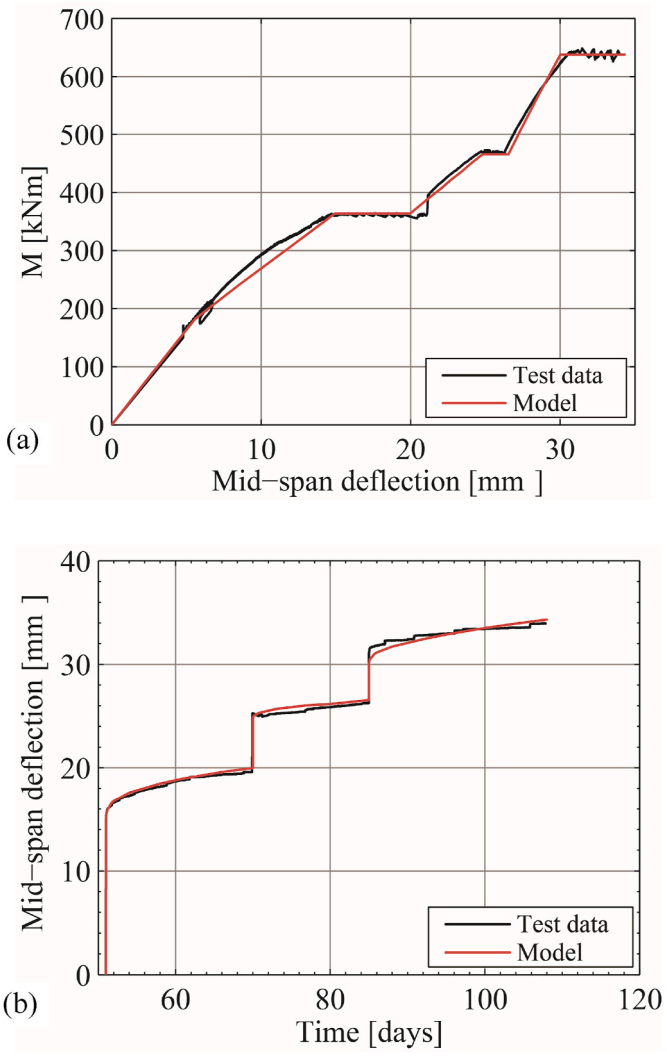

Fig. 14. Comparison between the experimental and the numerical moment vs. mid-span deflection (a) and mid-span deflection vs. time (b) curves for Beam-2.

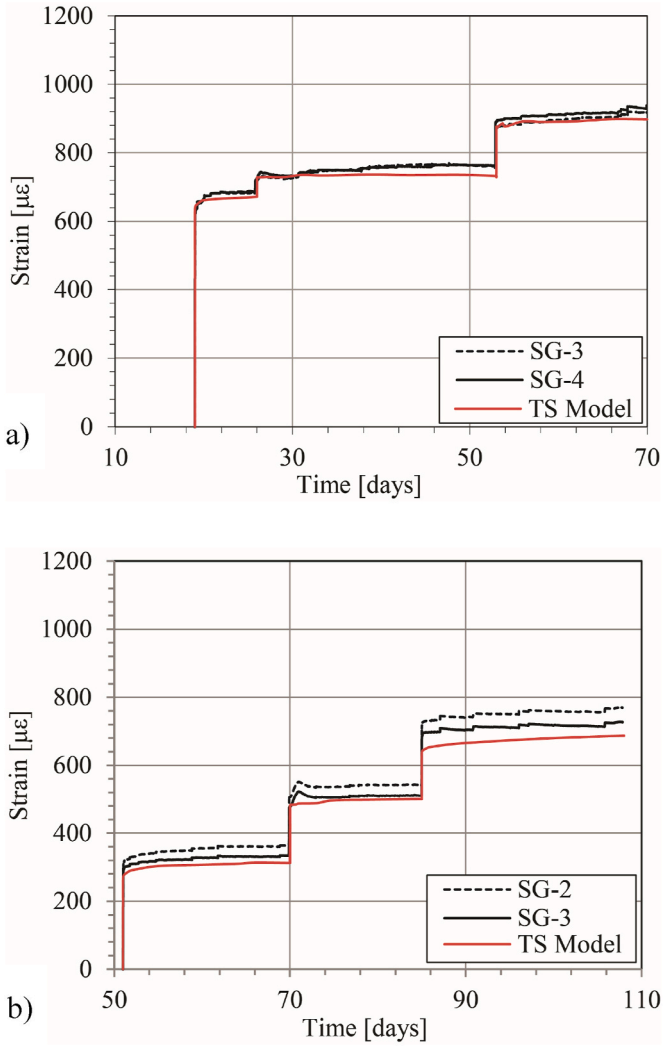

Fig. 15. Comparison among the strains the bottom rebar measured during the tests - see Fig. 1 for the strain gage (SG) locations - and computed through the tension stiffening (TS) model for beam-1 (a) and beam-2 (b).

provided an accurate estimate of the ultimate moment. Moment-curvature diagrams were then obtained to simulate the mid-span deflection development over time, also in this case the accuracy of the model was very high for one of the beams and slightly lower for the other, with an over-estimation of the mid-span deflection in the first half of the test. This is clearly a consequence of the reduced accuracy in the prediction of the moment curvature diagram. Finally, the numerical model was used to simulate the strain evolution over time in the tension reinforcement at mid-span. Also in this case a good accuracy was observed, even if the model tends to slightly underestimate the strains.

The model presented here can be effectively adopted to simulate the time-dependent behaviour of precast concrete beams completed with cast-in-place concrete. Further possible developments are related to the inclusion of thermal effects and of non-uniform shrinkage in the cross section.

Author statement

Nicola Buratti: Conceptualization, Formal analysis, Methodology, Software, Writing - Original Draft.

Claudio Mazzotti: Resources, Conceptualization, Experimental testing, Project administration, Methodology, Writing - Review & Editing.

Declaration of competing interest

The authors declare that they have no known competing financial interests or personal relationships that could have appeared to influence the work reported in this paper.

Appendix A. Supplementary data

Supplementary data to this article can be found online at https://doi.org/10.1016/j.jobe.2021.103176.

References

[1] Z.P. Bažant, Q. Yu, G.H. Li, Excessive long-time deflections of prestressed box girders. I: record-span Bridge in Palau and other paradigms, J. Struct. Eng. 138 (2012) 676–686.
[2] Z.P. Bažant, Q. Yu, G.H. Li, Excessive long-time deflections of prestressed box girders. II: numerical analysis and lessons learned, J. Struct. Eng. 138 (2012) 687–696.
[3] FIB, Model Code for Concrete Structures 2010, Ernst & Shon, 2013.
[4] A. Ghali, R. Favre, M. Elbadry, Concrete Structures: Stresses and Deformations: Analysis and Design for Sustainability, fourth ed., CRC Press, 2011.
[5] CEB, Serviceability Models, 1997.
[6] ACI Committee 209, Guide for Modeling and Calculating Shrinkage and Creep in Hardened Concrete, Framington Hills, 2008.

[7] R. Favre, J.-P. Jaccoud, O. Burdet, H. Charif, DIMENSIONNEMENT DES STRUCTURES EN BÉTON, Presses Polytechniques et Universitaires Romandes, 2004.
[8] Z.P. Bažant, Material models for structural creep analysis, in: Z.P. Bažant (Ed.), Mat. Model. Creep Shrinkage Concr., John Wiley & Sons Ltd, 1988, pp. 99–215.
[9] Z.P. Bažant, Viscoelasticity of solidifying porous material-concrete, J. Eng. Mech. Div. 103 (1977) 1049–1067.
[10] C. Mazzotti, M. Savoia, Nonlinear creep damage model for concrete under uniaxial compression, J. Eng. Mech. 129 (2003) 1065–1075, https://doi.org/10.1061/(ASCE)0733-9399(2003)129:9(1065).
[11] C. Mazzotti, A numerical model for the description of the long-term stress redistribution inside RC cross-sections completed in two stages, in: Proc. XX Conf. Ital. Soc. Appl. Mech., 12-15 September, Bologna, Italy, 2011.
[12] C. Mazzotti, M. Savoia, A Fiber Model for the Long-Term Behavior of Reinforced Concrete Sections. Creep, Shrinkage Durab. Mech. Concr. Concr. Struct. (CONCREEP 8), 30 September - 2 October, Ise-Shima, Japan, 2008, pp. 615–6121.
[13] N.C. Cluley, R. Shepherd, Analysis of concrete cable-stayed bridges for creep, shrinkage and relaxation effects, Comput. Struct. 58 (1996) 337–350, https://doi.org/10.1016/0045-7949(95)00131-Y.
[14] R.E. Erkmen, M.A. Bradford, Time-dependent creep and shrinkage analysis of composite beams curved in-plan, Comput. Struct. 89 (2011) 67–77, https://doi.org/10.1016/J.COMPSTRUC.2010.08.004.
[15] L. Jendele, D.V. Phillips, Finite element software for creep and shrinkage in concrete, Comput. Struct. 45 (1992) 113–126, https://doi.org/10.1016/0045-7949(92)90349-5.
[16] M.A. Pisani, Numerical analysis of creep problems, Comput. Struct. 51 (1994) 57–63, https://doi.org/10.1016/0045-7949(94)90036-1.
[17] M. Ferrari, Sistema costruttivo integrato, in: 15th Italian Conference CTE - Collegio dei Tecnici della Industrializzazione Edilizia, 1, 2004, pp. 815–822.
[18] J.J. Blandón, M.E. Rodríguez, Behavior of connections and floor diaphragms in seismic-resisting precast concrete buildings, Precast Concr Inst J 50 (2005) 56–75.
[19] C. Ceccoli, C. Mazzotti, M. Savoia, L. Vincenzi, M. Ferrari, Comportamento dei nodi del sistema di prefabbricazione APE, 16th Conf Ital "Collegio Dei Tec Della Ind Edil 1 (2006) 341–350.
[20] L. Vincenzi, C. Mazzotti, M. Savoia, C. Ceccoli, M. Ferrari, Investigation of ultimate capacity of beam-column joints of precast system, Stud Res 27 (2007) 93–116.
[21] M. Bottoni, C. Mazzotti, M. Savoia, Long-term experimental tests on precast beams completed with cast in situ concrete, Eur J Environ Civ Eng 13 (2009) 727–744, https://doi.org/10.1080/19648189.2009.9693148.
[22] P.J. Rabier, Some remarks on damage theory, Int. J. Eng. Sci. 27 (1989) 29–54, https://doi.org/10.1016/0020-7225(89)90166-3.
[23] Z.P. Bažant, S. Prasannan, Solidification theory for concrete creep. I: formulation, J. Eng. Mech. 115 (1989) 1691–1703, https://doi.org/10.1061/(ASCE)0733-9399(1989)115:8(1691).
[24] Z.P. Bažant, S. Prasannan, Solidification theory for concrete creep. II: verification and application, J. Eng. Mech. 115 (1989) 1704–1725, https://doi.org/10.1061/(ASCE)0733-9399(1989)115:8(1704).
[25] Z.P. Bažant, A. Hauggaard, S. Baweja, F. Ulm, Microprestress-solidification theory for concrete creep.I: aging and drying effects, J. Eng. Mech. 123 (1997) 1188–1194, https://doi.org/10.1061/(ASCE)0733-9399(1997)123:11(1188).
[26] Z.P. Bažant, A. Hauggaard, S. Baweja, Microprestress-solidification theory for concrete creep.II: algorithm and verification, J. Eng. Mech. 123 (1997) 1195–1201, https://doi.org/10.1061/(ASCE)0733-9399(1997)123:11(1195).
[27] I. Carol, Z. Bažant, Viscoelasticity with aging caused by solidification of nonaging constituent, J. Eng. Mech. 119 (1993) 2252–2269, https://doi.org/10.1061/(ASCE)0733-9399(1993)119:11(2252).
[28] O.C. Zienkiewicz, M. Watson, Some creep effects in stress analysis with particular reference to concrete pressure vessels, Nucl. Eng. Des. 4 (1966) 406–412, https://doi.org/10.1016/0029-5493(66)90069-0.
[29] Z.P. Bažant, S.T. Wu, Rate-type creep law of aging concrete based on maxwell chain, Mater. Construcción 7 (1974) 45–60, https://doi.org/10.1007/bf02482679.
[30] CEB, Design Manual on Cracking and Deformations, 1985.
[33] CEB, Structural Effects of Time-dependent Behaviour of Concrete, 1993.